MSDE

Molecular Systems Design & Engineering

rsc.li/molecular-engineering

Themed issue: MSDE Emerging Investigators 2020

ROYAL SOCIETY
OF CHEMISTRY

PAPER
Qian Chen *et al.*
Charting the quantitative relationship between
two-dimensional morphology parameters of
polyamide membranes and synthesis conditions

IChemE ADVANCING CHEMICAL ENGINEERING WORLDWIDE

Check for updates

Charting the quantitative relationship between two-dimensional morphology parameters of polyamide membranes and synthesis conditions†

Hyosung An, [ID] [ab] John W. Smith,[a] Wenxiang Chen,[ab] Zihao Ou [ID] [a] and Qian Chen [ID] *[abcd]

Polyamide membranes serve as the active layer in thin-film composites used for nanofiltration and reverse osmosis, and their surface morphology strongly impacts separation performance. However, because these surface morphologies are highly irregular and heterogeneous, linking morphology parameters to membrane synthesis conditions quantitatively is challenging. Here we utilize a quantitative morphometry approach, together with the surface feature classification scheme reported in our earlier work, to image and analyse the surface morphologies of polyamide membranes synthesized with a range of monomer concentrations. From transmission electron micrographs of polyamide membranes, we measure projected morphology parameters of "dome" and "dimple" crumples in the membrane, including surface curvature, Feret dimensions, thickness, circularity, perimeter, and area. All features except circularity, which remains constant, exhibit opposite trends when charted against the concentrations of *m*-phenylene diamine or trimesoyl chloride monomers used in synthesis suggesting competing roles of these two monomers in shaping crumples. Surprisingly, mathematical fittings (linear, logarithmic, or exponential) relate these morphology parameters quantitatively to the monomer concentration ratio, despite the apparent irregularity of crumples. Our highly quantitative approach sheds insight into predictive design of membrane materials with desirable properties.

Design, System, Application

Polyamide membranes have served as a standard active layer in thin-film composites used in the desalination industry for more than 30 years. However, because these membranes develop highly irregular surface features during synthesis, quantitative understanding of their synthesis–morphology relationship is limited, and efforts to achieve precise and rapid molecular separation have focused mainly on empirical engineering. Herein, we describe new avenues to quantify the complex morphology of polyamide membranes and thereby link their structure to synthesis conditions. We found that morphological parameters with respect to the monomer concentration ratio collapse onto unified curves: with an increasing amine to acyl chloride concentration ratio, crumple thickness, perimeter, and Feret distance increase and surface curvature decreases. Moreover, we demonstrated unified mathematical relationships to scale individual crumples as a function of morphological parameters across a wide range of reaction conditions. This report can help lay foundations for predictive design of advanced separation membranes, for capturing greenhouse gases, water treatment, and purification and recovery in pharmaceutical, petrochemical, and chemical industries.

Introduction

[a] Department of Materials Science and Engineering, University of Illinois at Urbana-Champaign, Urbana, Illinois 61801, USA. E-mail: qchen20@illinois.edu
[b] Materials Research Laboratory, University of Illinois at Urbana-Champaign, Urbana, Illinois 61801, USA
[c] Department of Chemistry, University of Illinois at Urbana-Champaign, Urbana, Illinois 61801, USA
[d] Beckman Institute for Advanced Science and Technology, University of Illinois at Urbana-Champaign, Urbana, Illinois 61801, USA

† Electronic supplementary information (ESI) available: TEM images of polyamide membranes; characterization of thickness and number density of polyamide crumples; morphological parameter fittings. See DOI: 10.1039/c9me00132h

Thin-film composite (TFC) membranes have been widely used in the water desalination industry for more than three decades.[1–3] TFC membranes generally consist of a polyester backing layer for physical support, a microporous polysulfone support midlayer, and a top layer of highly crosslinked and nanoporous polyamide membrane for selective molecular separation. The polyamide active layer is typically synthesized *via* polymerization at the interface of two immiscible phases: an aqueous phase containing an amine monomer and an organic phase containing an acyl chloride monomer (Fig. 1a). Upon contact of the two phases, the amine monomer in
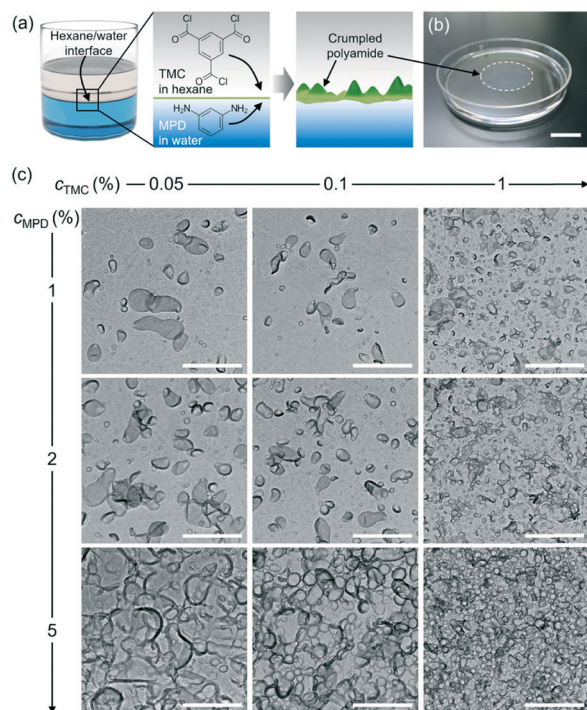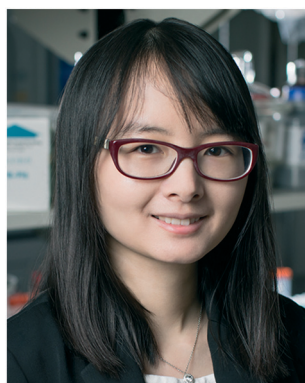
Fig. 1 (a) A schematic illustration of polyamide synthesis through polymerization at the interface between a water phase and an organic phase (hexane here). (b) A digital photo of a polyamide membrane floating on the water surface prepared with c_{MPD} of 1 w/v% and c_{TMC} of 1 w/v%. (c) TEM images of polyamide membranes with varying c_{MPD} (1–5 w/v%) and c_{TMC} (0.05–1 w/v%). The reaction time was 60 s. Scale bars: 20 mm in (b) and 500 nm in (c).

water can diffuse into the organic phase whereas the acyl chloride monomer is poorly soluble in water, so that polymerization occurs mostly on the organic side close to the

Qian Chen

Prof Qian Chen is an Assistant Professor in the Department of Materials Science and Engineering at the University of Illinois at Urbana-Champaign. The research in her group focuses on electron microscopy-based imaging, understanding and engineering of soft materials, such as nanoparticle and colloidal self-assembly, protein transformation, advanced battery materials and energy-efficient filtration. She has received awards for the research in her group such as the Victor LaMer award in ACS (2015), Forbes 30 under 30 Science List (2016), AFOSR YIP award (2017), NSF CAREER award (2018), Sloan Fellowship (2018), and the Unilever award in ACS (2018). More information on Prof. Qian Chen's group can be found at chenlab.matse.illinois.edu.

water–organic interface.[4–9] Subsequent polyamide film growth is self-limited because the diffusion of monomers is blocked by the grown film.[6,8,9] This polymerization reaction is rapid (*e.g.*, 50% of the final polyamide film forms within approximately 2 s)[10] and highly exothermic, generating heat at the water–organic interface.[11,12] The increase in temperature[13] and other factors such as rapid diffusion of amines into the organic phase after formation of an incipient layer[14] or generation of nanoscopic bubbles,[12] are speculated to be the origins of irregular membrane morphologies, such as ridge-and-valley structures and crumples.[13,15–17] For instance, polyamide films prepared by interfacial polymerization of trimesoyl chloride (TMC) and *m*-phenylene diamine (MPD) can exhibit a root-mean-square roughness as high as 80–120 nm due to crumple formation under certain synthesis conditions.[18] These surface morphological features such as film roughness and thickness have been shown to impact the solvent permeability, mass transport, solute rejection of polyamide films,[17,19,20] and sensitively depend on synthesis conditions such as monomer concentrations, support wettability, synthesis time, and temperature.[1,8,13,20–25] For example, Xu *et al.* reported on the effects of monomer concentrations on morphology characteristics such as nodular or leaf-like features as well as the pore sizes of polyamide membranes by using scanning and transmission electron microscopy (SEM, TEM).[26]

However, elucidating a quantitative and predictable, instead of empirical, relationship between the synthesis conditions and surface morphology of polyamide membranes remains challenging, despite its importance to the rational design of efficient membranes for various applications. Ensemble methods such as Rutherford backscattering spectroscopy,[10,27–30] microfluidic interferometry,[31] quartz crystal microbalance measurements,[32–35] Fourier transform infrared mapping spectroscopy,[36] time-domain thermoreflectance,[32] and spectroscopic ellipsometry[13,32,37] have been used to study polyamide membranes synthesized under different conditions, but cannot resolve their spatially irregular and heterogeneous surface morphology. For example, Matthews *et al.* used *in situ* diffuse reflectance and Rutherford Backscattering spectrometry to show the effects of monomer concentrations on polyamide growth kinetics and a relationship between the average roughness of the membrane and monomer concentration.[10] Recent applications of direct imaging methods such as TEM tomography[18,38,39] and focused ion beam SEM[40] have resolved the internal and surface morphology of polyamide films, but did not provide a quantified relationship between the membrane morphology and the synthesis conditions.

Here we integrate TEM imaging with quantitative morphometry of polyamide membranes synthesized with the TMC and MPD concentrations systematically varied, to quantify synthesis–morphology relationships. We explicitly demonstrate that by increasing MPD monomer concentration, the morphological parameters of the crumples (surface curvature, Feret distance, thickness, perimeter, and

area) are monotonically changed over a wide range. By increasing TMC monomer concentration, however, these morphological parameters are tuned in the opposite way. Interestingly, comparing the concentration ratio of MPD to TMC to these morphology parameters produces unified curves following either linear or exponential trends. The nanoscopic morphological parameters of individual crumples are macroscopically controlled as a function of synthesis conditions, which can potentially guide predictive design of polyamide membranes.

Experimental

Materials

Cadmium chloride hydrate (99.998%, CdCl$_2 \cdot x$H$_2$O, $x \approx$ 2.5, Alfa Aesar), ethanolamine (>98%, Sigma-Aldrich), m-phenylenediamine (MPD, 99%, Sigma-Aldrich), 1,3,5-benzenetricarbonyl trichloride (a.k.a. trimesoyl chloride, TMC, 98%, Sigma-Aldrich), molecular sieves (3 Å, 1–2 mm beads, Alfa Aesar), hydrochloric acid (36.5–38.0%, HCl, Macron), polysulfone film (PS35, Sepro Corporation), and methanol (99.9%, Fisher Chemical) were used as received without further purification. The organic phase hexane (99.9%, Fisher Chemical) was stored with approximately 225 g molecular sieves in a 1 L glass jar for 1 day before use. Water used in this work was purified by a Milli-Q Advantage A10 system (18.2 MΩ cm at 25 °C). All glassware was cleaned in a base bath (saturated potassium hydroxide in isopropyl alcohol), followed by an acid bath (1 M hydrochloric acid), fully rinsed with water, and dried with nitrogen gas. Note that cadmium chloride hydrate, MPD and TMC were carefully stored in a desiccator to prevent exposure to moisture, which is key for reproducible membrane synthesis.

Polyamide membrane synthesis

Polyamide films were synthesized with adaptations to a literature method[13] as described previously.[18] Cadmium hydroxide (Cd(OH)$_2$) nanowires were synthesized by sequential addition of aqueous solutions of CdCl$_2 \cdot x$H$_2$O (50 mL, 4 mM) and ethanolamine (50 mL, 2 mM) to a 250 mL Erlenmeyer flask stirring with a Teflon-coated magnetic bar (2 cm in length) at 500 rpm at room temperature. The solution turned cloudy and was stirred for 15 min. A polysulfone film was stored in water for at least 12 h to hydrate its pores. The hydrated polysulfone substrate (6 cm × 6 cm) was fixed on a glass filter funnel (5.7 cm outer diameter, 3.8 cm inner diameter) connected to a filtering flask, which was connected to a vacuum pump (KNF, UN726.3 FTP). The polysulfone substrate was washed by filtering methanol (20 mL), followed by filtering water (50 mL). The solution of cadmium hydroxide nanowires was filtered across the polysulfone substrate under vacuum (67 kPa). After the cadmium hydroxide nanowire solution was filtered, an aqueous solution of MPD with desired concentrations (from 1 to 5 w/v%) was gently transferred onto the polysulfone substrate using a 10 mL micropipette and

filtered under vacuum (67 kPa). The weight per volume percentage (*i.e.*, gram per mL, w/v%) is hereafter referred to as % for convenience. Immediately after this transfer, a TMC solution in hexane at desired concentrations (from 0.05 to 1%) was added and left on the polysulfone substrate to initiate interfacial polymerization. After 60 s, the TMC solution was gently removed using a micropipette and pure hexane (10 mL) was added to the polysulfone substrate to rinse away TMC and terminate the reaction. This rinsing step was repeated two more times. Immediately, the polysulfone substrate covered with the polyamide membrane was placed in a Petri dish (10 cm in diameter) filled with water. The polyamide membrane was released from the polysulfone substrate and floated at the air–water interface. The water in the Petri dish was replaced with HCl solution (10 mM). The floating polyamide membrane was kept soaking in the HCl solution overnight to remove any residue of cadmium hydroxide nanowires. The HCl solution was then replaced with water three times before the membrane was scooped up by a TEM grid for TEM imaging. Isolating and imaging the polyamide film from the polysulfone substrate serve our purpose better than studying the film with the substrate because the polysulfone substrate we used here are hundreds of microns thick, which precludes resolving any morphology details of the polyamide layer under projected-view TEM. As we presented here, the project-view TEM provides abundant information of convenient access to relate synthesis conditions with morphology details.

Polyamide film characterization by TEM

A JEOL 2100 Cryo TEM at an acceleration voltage of 200 kV was used for imaging the polyamide film morphology. Low electron dose rates (4.0–6.9 e$^-$ Å^{-2} s^{-1}) were applied using spot size 3 for TEM imaging to minimize beam-induced alteration of the membrane following our previous work.[18] We used carbon film-coated TEM grids (Electron Microscopy Sciences, CF400-Cu) to collect the polyamide membrane samples.

Quantitative morphometry analysis of polyamide membranes from TEM images

For the analysis, only visibly distinct single crumples that are either domes or dimples (identified based on our previous work[18]) were selected. Clustered crumples were not analysed due to the challenge to quantify their morphology parameters from projected two-dimensional (2D) TEM images. The TEM images were processed using FIJI software (1.52p version, National Institutes of Health).[41] We identified the crumples by first adjusting the image contrast using "Brightness/Contrast," applying a median filter with a radius of 3–4 pixels, and then applying a grey scale threshold to single out the crumples of low intensity and the contours of the crumples. A series of morphology parameters were next quantified based on the identified crumple contours at the single crumple level. The perimeter, area, maximum and minimum
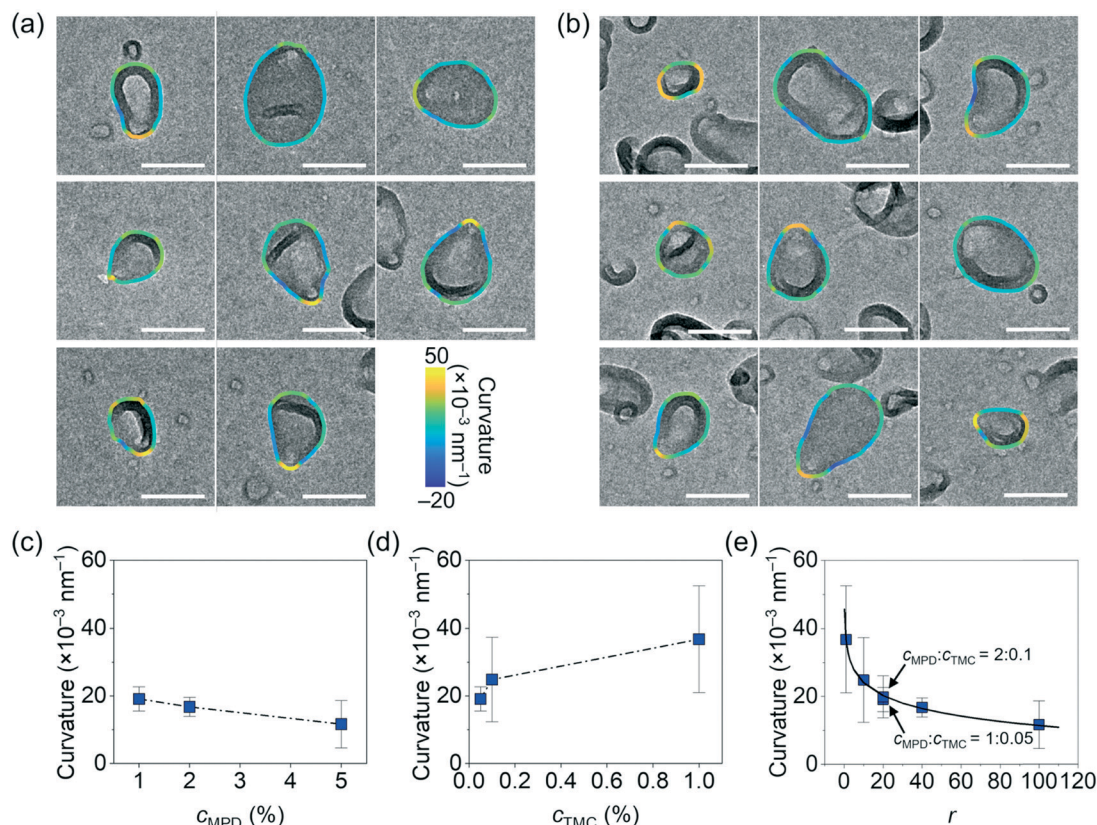
104 | *Mol. Syst. Des. Eng.*, 2020, **5**, 102–109

This journal is © The Royal Society of Chemistry 2020

Fig. 2 High-magnification TEM images of polyamide membranes prepared with (a) c_{MPD} of 1% and c_{TMC} of 0.05% and (b) c_{MPD} of 2% and c_{TMC} of 0.1%. The TEM images were overlaid with surface contour colour coded according to local surface curvature. Average local surface curvature as a function of (c) c_{MPD} with fixed c_{TMC} (0.05%), (d) c_{TMC} with fixed c_{MPD} (1%), and (e) the concentration ratio of MPD to TMC ($r = c_{MPD}/c_{TMC}$). The black dot-dashed lines in (c) and (d) are to guide the eye. The black solid line in (e) presents a logarithmic fit of curvature (in μm^{-1}) = $-5.5 \ln(r) + 36.7$ with $R^2 = 0.99$. Scale bars: 100 nm in (a) and (b).
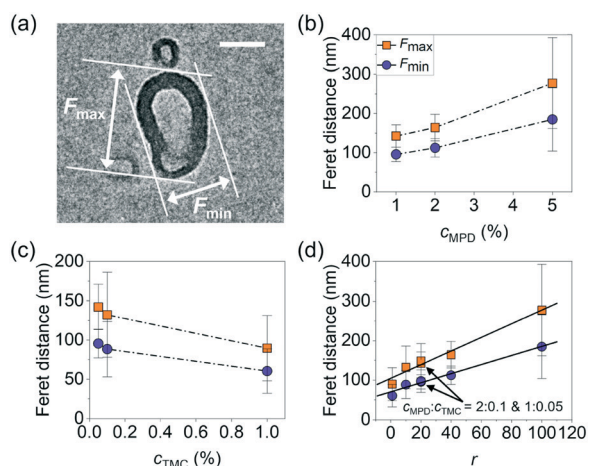

Fig. 3 (a) Analysis of maximum and minimum Feret distances of a representative crumple in a polyamide membrane synthesized with c_{MPD} of 1% and c_{TMC} of 0.05%. Average maximum and minimum Feret distances as a function of (b) c_{MPD} with fixed c_{TMC} (0.05%), (c) c_{TMC} with fixed c_{MPD} (1%), and (d) the concentration ratio of MPD to TMC r. The black dot-dashed lines in (b) and (c) are guide to the eye. The black solid lines in (d) present the linear scaling F_{max} (in nm) = $1.7r + 104.5$ with $R^2 = 0.98$ and F_{min} (a unit of nm) = $1.2r + 70.2$ with $R^2 = 0.98$. Scale bar: 50 nm in (a).

Feret distances (F_{max} and F_{min}, *i.e.*, the longest and the shortest distances between two parallel lines restricting the boundary of each crumple, Fig. 3a), and circularity ($4\pi \times$ (area)/(perimeter)^2) of the crumples were measured using the BioVoxxel image processing and analysis toolbox for ImageJ. As for local curvature at each pixel of the crumple contour, it is defined and measured as the inverse of the radius of the best-fitted circle to the local arc (smoothed by 10 pixels, 6.8 nm; fitted by 50 pixels, 34.1 nm) containing the pixel. The local curvature analysis was conducted following the protocols detailed in our previous study.[42,43] As for crumple thickness, we drew lines across crumple contours, plotted the grey intensity of a TEM image along the distance, and then measured the thickness of crumples. A total of 66 crumples (at least 8 for each reaction condition, see Fig. 2a and b and S1 and S2†) were measured.

Results and discussion

To study the relationship between the surface morphology of polyamide membranes and their synthesis conditions, we prepared a total of nine polyamide membrane samples following methods detailed above by varying the MPD (c_{MPD}, 1–5%) and TMC (c_{TMC}, 0.05–1%) concentrations, with the

This journal is © The Royal Society of Chemistry 2020

Mol. Syst. Des. Eng., 2020, **5**, 102–109 | **105**

reaction time fixed at 60 s. Fig. 1b shows a photograph of a representative free-standing polyamide film floating on the water surface. The film was then gently scooped onto a TEM grid and dried in air for TEM imaging. As shown in Fig. 1c, the polyamide membranes clearly exhibit irregularly shaped and heterogeneous crumples, with differences in the crumple morphology depending on the MPD and TMC concentration(s). For example, an increase in the concentrations of either MPD or TMC leads to an increase in the number density of crumples (Fig. S3†). A higher c_{MPD} increases the crumple size slightly, whereas a higher c_{TMC} decreases the crumple size (Fig. 1c), suggesting competition between these two monomers likely due to their solubility anisotropy.[31,44] The MPD molecules can diffuse deep into the hexane phase to grow large crumples, while TMC molecules with low solubility in the water phase react rapidly with MPD at the water–hexane interface into a self-limited polyamide film, consistent with previous work showing polyamide film growth is limited by MPD diffusion.[6,31,45,46] To further understand the effect of monomer concentrations on crumple morphologies, we quantified a series of crumple structure parameters as detailed below.

We first quantified the overall anisotropic shape of the crumples using local surface curvature and Feret distance following the method detailed above, both of which show opposite trends as the MPD and TMC concentrations change. Here the surface curvature of a pixel at the crumple contour is defined as the inverse of the radius of the best-fitted circle to the local arc containing the pixel. Fig. 2a and b shows zoomed-in TEM views of single crumples overlaid by their contour coloured to local surface curvature values. We applied this analysis to different polyamide membranes (at least 8 single crumples were counted for each membrane, Fig. S1 and S2†). As plotted in Fig. 2c, as c_{MPD} increases from 1% to 5% at a fixed c_{TMC} (0.05%), the average local surface curvature decreases from $(19 \pm 4) \times 10^{-3}$ nm^{-1} to $(14 \pm 6) \times 10^{-3}$ nm^{-1}. The TMC concentration effect shows an opposite trend (Fig. 2d): the average local curvature increases from $(14 \pm 6) \times 10^{-3}$ nm^{-1} to $(37 \pm 16) \times 10^{-3}$ nm^{-1} as the c_{TMC} increases from 0.05% to 1% at a fixed c_{MPD} (1%). It may suggest that a higher c_{TMC} at the hexane phase results in the earlier termination of crumple growth probably due to faster consumption of diffused MPD in the presence of a high concentration of TMC. Meanwhile, the Feret distances (F_{max}, F_{min}) of crumples measure how far the projected 2D view of the crumple shape deviates from a circle (Fig. 3a). As the c_{MPD} increases from 1% to 5%, the average Feret distances monotonically increase, from 142 to 277 nm for F_{max} and from 96 to 185 nm for F_{min} (Fig. 3b) at a fixed c_{TMC} (0.05%). In comparison, as we increase c_{TMC} from 0.05% to 1%, the average Feret distances decrease, from 142 to 90 nm for F_{max} and from 96 to 60 nm for F_{min} (Fig. 3c) at a fixed c_{MPD} (1%), suggesting the faster consumption of diffused MPD with higher c_{TMC} in hexane. These results confirm again the two monomers have a competing effect on the crumple formation, which is suggested elsewhere.[21,25,26,47]

The competing dependence of the local surface curvature and Feret distances on c_{MPD} and c_{TMC} motivates us to plot these two parameters as a function of the concentration ratio of MPD to TMC ($r = c_{MPD}/c_{TMC}$). Both parameters fall onto consistent mathematical fitting forms. The average local surface curvature of the crumples logarithmically decays as r increases ($R^2 = 0.99$, Fig. 2e). Interestingly, the two polyamide membrane samples synthesized at the same concentration ratio r of 20 but different monomer concentrations (1% MPD + 0.05% TMC vs. 2% MPD + 0.1% TMC) collapse nicely onto this fitting with similar curvatures (($1.9 \pm 0.4) \times 10^{-2}$ nm^{-1} vs. $(2.0 \pm 0.6) \times 10^{-2}$ nm^{-1}, respectively as highlighted in Fig. 2e). The average F_{max} and F_{min} of crumples follow a linear increase as a function of r ($R^2 = 0.98$, Fig. 3d), while the data from the two samples synthesized at the same r again matches with the fitting. These results indicate that the concentration ratio of MPD to TMC plays a role in the formation of crumple structures, charting a one-to-one relationship with the surface curvature and Feret distances of the crumples. Note that surface curvature and Feret distance directly relate to various parameters governing film transport
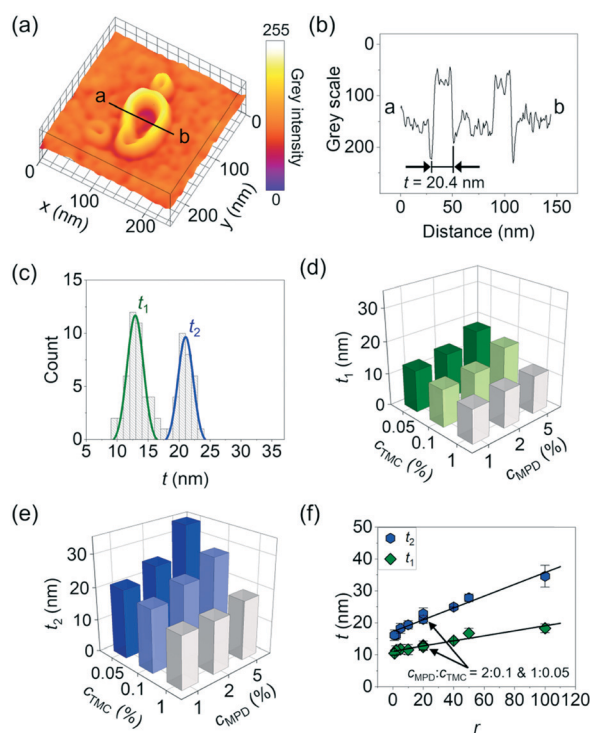

Fig. 4 (a) Grey intensity plot of a TEM image of a representative crumple in polyamide membrane synthesized with c_{MPD} of 1% and c_{TMC} of 0.05%. The three-dimensional (3D) plot was colour-coded according to the grey scale. (b) Grey scale intensity plotted along the black line noted in Fig. 4a, showing the thickness of a representative crumple t of 20.4 nm. (c) A histogram of crumple thickness of the polyamide membrane synthesized with c_{MPD} of 1% and c_{TMC} of 0.05%. Average crumple thickness of (d) t_1 and (e) t_2 as a function of c_{MPD} and c_{TMC}. (f) Average crumple thickness as a function of the concentration ratio of MPD to TMC r. The black solid lines are linear fittings yielding slopes of 0.08 ($R^2 = 0.98$) and 0.19 ($R^2 = 0.98$) for t_1 and t_2, respectively.

properties, such as effective permeable area, surface-to-volume ratio, mass-per-area, local charge density, and local pK_a of acidic ligands.[13,18,48,49] For example, in one study, the crumpled morphology of a polyamide membranes provided higher permeance than that of a flat membrane by a factor of 4 owing to its higher effective permeable area.[13] In our previous work, different crumple morphologies display distinct microenvironments as confirmed by ion adsorption tests using energy dispersive X-ray spectroscopy in a scanning transmission electron microscope.[18]

Beyond the above parameters that characterize the shape anisotropy of the crumples, we next measured the crumple thickness t that directly relates to solvent permeation length involved in molecular separation[50,51] and mechanical stability required for the high operating pressures for reverse osmosis and nanofiltration.[13,14,19,26] For this measurement, we plotted the grey scale intensity of a TEM image across a crumple (see the example in Fig. 4a and b, sample prepared with 1% MPD + 0.05% TMC). We repeated the measurement for 8 crumples synthesized at this condition, the distribution of which exhibits a clear bi-modal shape ($t_1 = 13 \pm 1$ nm; $t_2 = 21 \pm 1$ nm, Fig. 4c), consistent with our previous work when both dome and dimpled crumples were counted.[18] Likewise, the polyamide membranes synthesized at other c_{MPD} and c_{TMC} show bi- or multi-modal distribution of the crumple

thickness t (Fig. S4†). For ease of discussion, we plotted t_1 and t_2 vs. the monomer concentrations, and both thicknesses increase as c_{MPD} increases (Fig. 4d and e and S5†) and decrease as c_{TMC} increases (Fig. 4d and e and S5†), again confirming the competing effects of MPD and TMC on crumple formation. Similarly, the average area and perimeter of crumples show the opposite trends as the MPD and TMC concentrations change whereas circularity remains constant (Fig. S6†).

When it comes to the dependence on the concentration ratio of MPD to TMC r, both t_1 and t_2 again fall into a unified mathematical form, scaling linearly to r ($R^2 = 0.98$ for both, Fig. 4f). These results show that the monomer concentration ratio r serves as a potent handle for a one-to-one prediction of the membrane crumple thickness. The slope of the t_2–r curve is larger than that of the t_1–r curve, suggesting the formation of the thinner film is the rate-limiting step in the morphology development of the membrane. This observation is consistent with a crumpling mechanism identified in earlier studies where a uniform polymer sheet is formed first during interfacial polymerization and subsequently collapsed locally to form crumples.[14,19,26,37]

While the above quantitative and monotonic relationship linking these surface morphology parameters (e.g., surface curvature, Feret distances, thickness) to r can serve as a
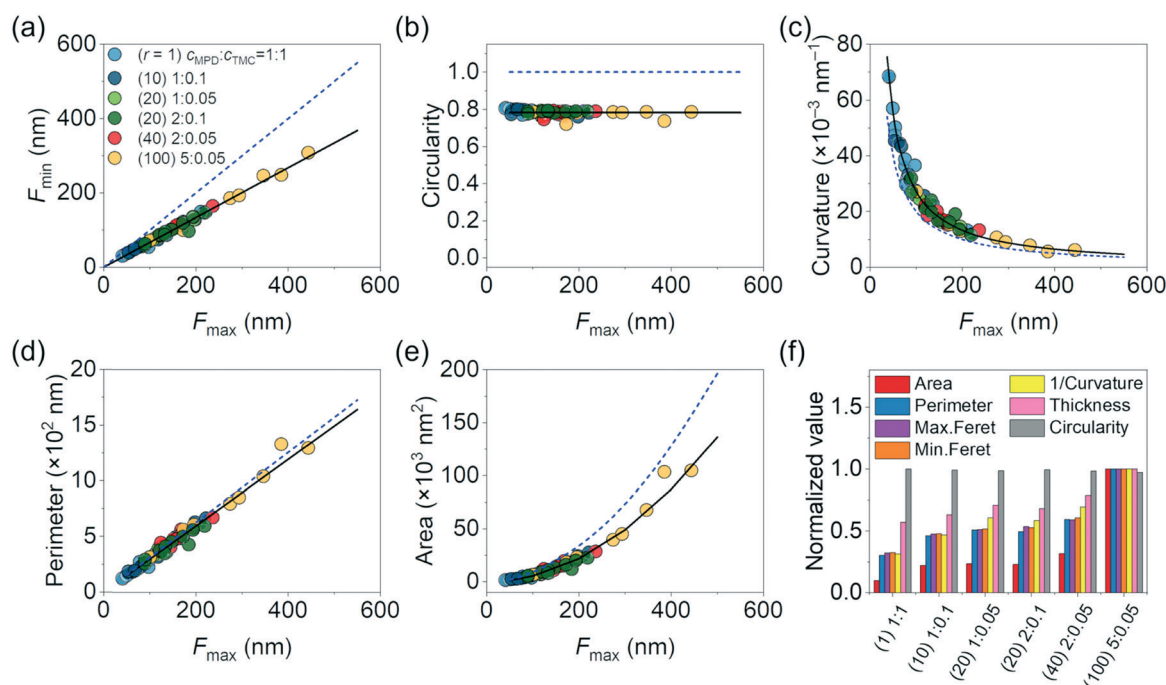

Fig. 5 Plots of (a) minimum Feret distance, (b) circularity, (c) curvature, (d) perimeter, and (e) projected area of crumples as a function of maximum Feret distance. The dashed blue lines are the scaling of perfect circular shape: $F_{min} = F_{max}$ (units of nm) in (a); circularity = 1 in (b); curvature (a unit of μm^{-1}) = $2 \times (F_{max})^{-1}$ in (c); perimeter (a unit of nm) = $\pi \times (F_{max})$ in (d); and area (a unit of nm^2) = $\pi \times (F_{max}/2)^2$ in (e). The black solid lines are fittings with a linear fit yielding a slope of 0.67 with $R^2 = 0.99$ in (a); an average circularity of 0.78 in (b); a power law fit yielding curvature (a unit of μm^{-1}) = $3.1 \times (F_{max})^{-1.03}$ with $R^2 = 0.98$ in (c); a linear fit yielding perimeter (a unit of nm) = $0.95\pi \times (F_{max})$ with $R^2 = 0.98$ in (d); and a power-law fit yielding area (a unit of nm^2) = $\pi \times (F_{max}/2.4)^2$ with $R^2 = 0.98$ in (e), all confirming elongated structure of crumples. (f) Distribution of morphological characteristics normalized to the maximum value of each parameter across the samples. In the label of x-axis, polyamides with the ratio "j" of c_{MPD} and c_{TMC}, "k"% MPD, and "l"% TMC are expressed as "(j)k:l". At least 8 crumples for each membrane were analysed (Fig. S1 and S2†).

This journal is © The Royal Society of Chemistry 2020

Mol. Syst. Des. Eng., 2020, 5, 102–109 | 107

working curve to guide synthesis, we find that these parameters also follow universal scaling laws for the polyamide samples synthesized with varied monomer concentrations and seemingly disparate in structure (Fig. 5). We plotted collectively the data on F_{min}, circularity, curvature, perimeter, and area of a total of 66 crumples (Fig. S1 and S2,† at least 8 crumples for each of the membranes synthesized) against F_{max} (Fig. 5a–e). Here the x-axis of F_{max} is arbitrarily chosen; the scaling works for any pairs of two morphology parameters. Note that the values of the morphology parameters vary by an order of magnitude or more across the 66 crumples of the 6 samples synthesized at different monomer concentrations: from 41 to 445 nm for F_{max}, from 5×10^{-3} to 6.8×10^{-2} nm^{-1} for local surface curvature, from 116 to 1327 nm for perimeter, and from 8.6×10^2 to 1.0×10^5 nm^2 for area (Fig. 5a–e). Out of this large parameter space we sampled, the morphology parameters consistently scale relative to each other. For instance, F_{min} scales linearly to F_{max} across all the polyamide membranes ($R^2 = 0.99$, Fig. 5a) with the slope of 0.67 measuring the extent of elongation in the crumples (a perfect circular shape has a slope of 1). This constant extent of elongation is consistent with the circularity measurement, which presents average circularity of 0.78 with narrow standard deviation of 0.01 across the samples (Fig. 5b). The surface curvature of the crumple scales with a power law of exponent −1.03 to F_{max} ($R^2 = 0.98$, Fig. 5c), where an exponent of −1 is expected for a perfect circle. Similar fittings work for other morphology parameters such as perimeter and area of the crumple (Table S1†). The correlations of the various morphological parameters suggest that crumple growth follows unified morphology–synthesis relations.

Lastly, we summarize all the morphological properties of different crumples in Fig. 5f. For convenient comparison in trends, we used inverse curvature. Morphological parameters are normalized to the maximum value of each one across the samples. All normalized parameters gradually increased with an increasing concentration ratio of MPD to TMC (r). The two polyamide films with the same concentration ratio r of 20 but different c_{MPD} and c_{TMC} (1% MPD + 0.05% TMC vs. 2% MPD + 0.1% TMC) had highly similar values across all crumple morphology parameters (Fig. 5f), similar to those observed elsewhere.[32] The results are in agreement with our predictions of MPD–TMC competition and support the idea that reactant ratios dictate crumple structure. It is noted that our previous study investigated crumple structure in 3D.[18] Thus, further studies on 3D morphological parameters such as crumple height are needed to fully understand crumpling mechanisms and structure–synthesis correlation of polyamide membranes.

Conclusions

In summary, using our morphometry platform we demonstrated that crumpled polyamide films follow quantitative synthesis–morphology relationships. We compared a series of polyamide films with varied amine and acyl chloride monomer concentrations with fixed reaction time of 60 s. Our results are consistent with an hypothesis that the crumple growth process is the result of competition between the amine monomer in the water phase and the acyl chloride monomer in the organic phase (MPD vs. TMC). The concentrations of the two monomers tune crumple morphological parameters such as surface curvature, Feret distance, thickness, perimeter, and area monotonically but in the reverse directions. Such a competition process between two monomers was further supported by scaling morphological parameters as a function of the concentration ratio of MPD to TMC ($r = c_{MPD}/c_{TMC}$). Furthermore, we found a unified mechanistic principle of crumple formation where the individual crumples, although seemingly unrelated in shape, can be scaled as a function of morphological properties. We anticipate that this morphometry platform can be applicable to other nanoscale soft materials and provides engineering strategies based directly on synthesis–morphology–function relationships.

Conflicts of interest

There are no conflicts to declare.

Acknowledgements

References

1 M. R. Chowdhury, J. Steffes, B. D. Huey and J. R. McCutcheon, *Science*, 2018, **361**, 682–686.
2 M. Elimelech and W. A. Phillip, *Science*, 2011, **333**, 712–717.
3 R. Larson, J. Cadotte and R. Petersen, *Desalination*, 1981, **38**, 473–483.
4 V. Freger, *Langmuir*, 2005, **21**, 1884–1894.
5 Y. Zhang, N. E. Benes and R. G. Lammertink, *Lab Chip*, 2015, **15**, 575–580.
6 G.-Y. Chai and W. B. Krantz, *J. Membr. Sci.*, 1994, **93**, 175–192.
7 J. Wang, R. Xu, F. Yang, J. Kang, Y. Cao and M. Xiang, *J. Membr. Sci.*, 2018, **556**, 374–383.
8 Y. Suzuki, Y. Koyano and M. Nagaoka, *J. Phys. Chem. B*, 2015, **119**, 6776–6785.
9 J. Muscatello, E. Müller, A. Mostofi and A. Sutton, *J. Membr. Sci.*, 2017, **527**, 180–190.
10 T. D. Matthews, H. Yan, D. G. Cahill, O. Coronell and B. J. Mariñas, *J. Membr. Sci.*, 2013, **429**, 71–80.
11 B. Ukrainsky and G. Z. Ramon, *J. Membr. Sci.*, 2018, **566**, 329–335.

12 X.-H. Ma, Z.-K. Yao, Z. Yang, H. Guo, Z.-L. Xu, C. Y. Tang and M. Elimelech, *Environ. Sci. Technol. Lett.*, 2018, **5**, 123–130.

13 S. Karan, Z. Jiang and A. G. Livingston, *Science*, 2015, **348**, 1347–1351.

14 H. Yan, X. Miao, J. Xu, G. Pan, Y. Zhang, Y. Shi, M. Guo and Y. Liu, *J. Membr. Sci.*, 2015, **475**, 504–510.

15 F. A. Pacheco, I. Pinnau, M. Reinhard and J. O. Leckie, *J. Membr. Sci.*, 2010, **358**, 51–59.

16 C. Y. Tang, Y.-N. Kwon and J. O. Leckie, *J. Membr. Sci.*, 2007, **287**, 146–156.

17 A. K. Ghosh, B.-H. Jeong, X. Huang and E. M. Hoek, *J. Membr. Sci.*, 2008, **311**, 34–45.

18 X. Song, J. W. Smith, J. Kim, N. J. Zaluzec, W. Chen, H. An, J. M. Dennison, D. G. Cahill, M. A. Kulzick and Q. Chen, *ACS Appl. Mater. Interfaces*, 2019, **11**, 8517–8526.

19 M. Hirose, H. Ito and Y. Kamiyama, *J. Membr. Sci.*, 1996, **121**, 209–215.

20 X. Ma, Z. Yang, Z. Yao, H. Guo, Z. Xu and C. Y. Tang, *J. Colloid Interface Sci.*, 2019, **540**, 382–388.

21 B. Khorshidi, T. Thundat, B. A. Fleck and M. Sadrzadeh, *Sci. Rep.*, 2016, **6**, 22069.

22 X. Li, Q. Li, W. Fang, R. Wang and W. B. Krantz, *J. Membr. Sci.*, 2019, **580**, 12–23.

23 J. E. Gu, S. Lee, C. M. Stafford, J. S. Lee, W. Choi, B. Y. Kim, K. Y. Baek, E. P. Chan, J. Y. Chung and J. Bang, *Adv. Mater.*, 2013, **25**, 4778–4782.

24 S. Gao, Y. Zhu, Y. Gong, Z. Wang, W. Fang and J. Jin, *ACS Nano*, 2019, **13**(5), 5278–5290.

25 B. Khorshidi, T. Thundat, B. Fleck and M. Sadrzadeh, *RSC Adv.*, 2015, **5**, 54985–54997.

26 J. Xu, H. Yan, Y. Zhang, G. Pan and Y. Liu, *J. Membr. Sci.*, 2017, **541**, 174–188.

27 O. Coronell, B. J. Mariñas, X. Zhang and D. G. Cahill, *Environ. Sci. Technol.*, 2008, **42**, 5260–5266.

28 O. Coronell, M. I. González, B. J. Mariñas and D. G. Cahill, *Environ. Sci. Technol.*, 2010, **44**, 6808–6814.

29 O. Coronell and D. G. Cahill, *Environ. Sci. Technol.*, 2009, **43**, 5042–5048.

30 O. Coronell, B. J. Marinas and D. G. Cahill, *Environ. Sci. Technol.*, 2011, **45**, 4513–4520.

31 A. Nowbahar, V. Mansard, J. M. Mecca, M. Paul, T. Arrowood and T. M. Squires, *J. Am. Chem. Soc.*, 2018, **140**, 3173–3176.

32 J. M. Dennison, X. Xie, C. J. Murphy and D. G. Cahill, *ACS Appl. Nano Mater.*, 2018, **1**, 5008–5018.

33 X. Song, S. Qi, C. Y. Tang and C. Gao, *J. Membr. Sci.*, 2017, **540**, 10–18.

34 L. A. Perry and O. Coronell, *J. Membr. Sci.*, 2013, **429**, 23–33.

35 D. L. Shaffer, M. E. Tousley and M. Elimelech, *J. Membr. Sci.*, 2017, **525**, 249–256.

36 D. Ren, J. I. N. Yeo, T.-Y. Liu and X. Wang, *Polym. Chem.*, 2019, **10**, 2769–2773.

37 L. Lin, R. Lopez, G. Z. Ramon and O. Coronell, *J. Membr. Sci.*, 2016, **497**, 365–376.

38 F. Pacheco, R. Sougrat, M. Reinhard, J. O. Leckie and I. Pinnau, *J. Membr. Sci.*, 2016, **501**, 33–44.

39 T. E. Culp, Y.-X. Shen, M. Geitner, M. Paul, A. Roy, M. J. Behr, S. Rosenberg, J. Gu, M. Kumar and E. D. Gomez, *Proc. Natl. Acad. Sci. U. S. A.*, 2018, **115**, 8694–8699.

40 M. M. Kłosowski, C. M. McGilvery, Y. Li, P. Abellan, Q. Ramasse, J. T. Cabral, A. G. Livingston and A. E. Porter, *J. Membr. Sci.*, 2016, **520**, 465–476.

41 J. Schindelin, I. Arganda-Carreras, E. Frise, V. Kaynig, M. Longair, T. Pietzsch, S. Preibisch, C. Rueden, S. Saalfeld and B. Schmid, *Nat. Methods*, 2012, **9**, 676.

42 J. Kim, X. Song, A. Kim, B. Luo, J. W. Smith, Z. Ou, Z. Wu and Q. Chen, *Macromol. Rapid Commun.*, 2018, **39**, 1800101.

43 Z. Ou, X. Song, W. Huang, X. Jiang, S. Qu, Q. Wang, P. V. Braun, J. S. Moore, X. Li and Q. Chen, *ACS Appl. Mater. Interfaces*, 2018, **10**, 40990–40995.

44 P. W. Morgan and S. L. Kwolek, *J. Polym. Sci.*, 1959, **40**, 299–327.

45 Y. Jin and Z. Su, *J. Membr. Sci.*, 2009, **330**, 175–179.

46 J. Ji and M. Mehta, *J. Membr. Sci.*, 2001, **192**, 41–54.

47 M. Rastgar, A. Shakeri and H. Salehi, *Environ. Sci. Pollut. Res.*, 2019, **26**, 1181–1191.

48 D. A. Walker, E. K. Leitsch, R. J. Nap, I. Szleifer and B. A. Grzybowski, *Nat. Nanotechnol.*, 2013, **8**, 676.

49 Z. Tan, S. Chen, X. Peng, L. Zhang and C. Gao, *Science*, 2018, **360**, 518–521.

50 J. G. Wijmans and R. W. Baker, *J. Membr. Sci.*, 1995, **107**, 1–21.

51 G. M. Geise, H. B. Park, A. C. Sagle, B. D. Freeman and J. E. McGrath, *J. Membr. Sci.*, 2011, **369**, 130–138.

This journal is © The Royal Society of Chemistry 2020

Mol. Syst. Des. Eng., 2020, **5**, 102–109 | 109